Finite Elements in Analysis and Design 224 (2023) 103985

Contents lists available at ScienceDirect

Finite Elements in Analysis & Design

journal homepage: www.elsevier.com/locate/finel

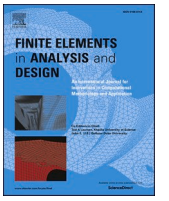

Geometry correction factor polynomials for corner crack test pieces accounting for constrained boundary conditions

Stephen Williams

Institute of Structural Materials, Swansea University, Fabian Way, Swansea SA1 8EN, United Kingdom

ARTICLE INFO

Keywords:
Finite element analysis
J-integral
Stress intensity factor
Constraint effects

ABSTRACT

The calculation of stress intensities used when processing growth data from fatigue tests on corner crack test pieces typically uses geometry correction factor polynomials derived from 3D finite element (FE) analyses with a remote applied load but no controls on nodal displacements. The built-in threaded ends of the test pieces, however, impose a constraint that results in significantly lower correction factors for large cracks than given by those polynomials.

This paper presents new geometry correction factor polynomials that are suitable for all corner crack test pieces with a square cross-section gauge region that blends via constant radius fillets into threaded ends. The polynomials are expressed as a function of the key test piece dimensions.

The individual FE analyses used to derive the correction factor polynomials were run on constant cross-section models containing quarter-circular notches with a 10 μm tip radius. The constraints applied to the loaded end of the models make the J-integral (and hence K) values sensitive to the overall model length. Consequently, a method based on matching bending stiffnesses was derived to understand how to adjust the model length to represent the stiffer fillet regions between the gauge section and the grips. The suitability of this approach was confirmed by performing a limited number of analyses on models that also contained the fillet and grip regions.

1. Introduction

Corner crack growth tests are usually conducted using threaded test pieces having designs similar to that shown schematically in Fig. 1. The test piece is symmetrical about the central plane AA, which contains a starter slit in one corner from which a quarter-circular crack is grown under cyclic loading conditions.

During cyclic testing, crack lengths a can be determined by a number of methods including Potential Drop (PD). Growth rates da/dN are then most often plotted against the stress intensity K. The stress intensities are calculated based on the nominal section stress σ (applied load/uncracked cross-sectional area), the crack length and a geometry correction factor Y.

The geometry correction factor polynomials for corner cracks derived by Pickard [1], Newman and Raju [2] and Raju and Newman [3] have been used both for processing test data [4–7] and as datums to compare with bespoke K calculations for specific test piece or crack geometries [8–10].

The correction factors in Refs. [1–3] were calculated using results from 3D Finite Element (FE) models with loads applied to the end furthest from the crack plane but, crucially, no controls on the nodal displacements in that region. This is not appropriate for test pieces with threaded ends, which will constrain planes normal to the specimen axis in the threaded regions to remain parallel to the crack

E-mail address: 2031771@swansea.ac.uk.

https://doi.org/10.1016/j.finel.2023.103985
Received 7 December 2022; Received in revised form 21 April 2023; Accepted 24 May 2023
Available online 7 July 2023

Nomenclature

a	crack length
$a_{n\ x}$	Term in overall correction factor polynomial x degrees around the crack front. n = 0, 2, 4
α_x	Parameter associated with tanh fit to correction factor as a function of 3D model length
β_x	Parameter associated with tanh fit to correction factor as a function of 3D model length
d	Test piece thickness a distance x along its length
δ	Beam deflection
D	test piece grip diameter
d_0-d_2	Parameters describing how effective 3D model length varies with test piece grip diameter
da/dN	crack growth rate per cycle
E	Young's modulus
FE	Finite Element
I	Moment of area
J	J-integral
K	stress intensity factor
L	Length of parallel sided beam
L_{3D}	Length of 3D finite element model
L_{EQ3D}	Equivalent length of 3D finite element model after scaling to test piece datum width of 7 mm
L_g	length of parallel gauge section of test piece
L_{LFACx}	Factor for model length in geometry correction factor polynomials
L_x	Length term in tanh fit to correction factor as a function of 3D model length
l_0-l_3	Parameters describing how effective 3D model length varies with test piece gauge length
M_B	Back face factor in Pickard geometry correction factor polynomials
M_G	Bending moment at test piece grips
M_{GP}	General factor in Pickard geometry correction factor polynomials
M_S	Side face factor in Pickard geometry correction factor polynomials
$M_{(x)}$	Bending moment along beam as a function of axial distance x
N	Number of cycles
ν	Poisson's ratio
O_1	Overall parameter in equations relating effective 3D model length to test piece dimensions
P	Point load
PD	Potential Drop
r	fillet radius between test piece parallel gauge section and grips, radial distance from crack tip
r_0-r_2	Parameters describing how effective 3D model length varies with test piece fillet radius
σ	direct stress
VB	Visual Basic
w	thickness of test piece parallel gauge section
w_{act}	Actual 3D model width
w_{datum}	Datum 3D model width
x	Axial distance along test piece
x_0	axial distance between end of parallel gauge section and start of test piece threads
Y	crack geometry correction factor
$Y0$	surface geometry correction factor
$Y45$	geometry correction factor 45° around the quarter-circular crack front
$Y_{LFAC}\ x$	model length correction factor as a function of 3D model length at crack front location x
$Y_L\ x$	correction factor as a function of 3D model length at crack front location x
$Y_{x\ FIXED}$	Overall correction factor x degrees around the crack front, constrained boundary conditions
$Y_{x\ FREE}$	Overall correction factor x degrees around the crack front, unconstrained boundary conditions

plane. This in turn has implications for the accuracy of EN 3873 [4], the European standard on determining fatigue crack growth rates using corner cracked test pieces.

This study runs FE analyses on different corner crack test piece geometries with and without end constraints to understand how these affect correction factor values for different crack lengths. Constant cross-section 3D models of half the test piece were used, with the cracks being represented as quarter-circular notches with a 10 μm tip radius. Because the constraints applied to the loaded end of the models make the J-integral (and hence K) values sensitive to the overall model length, a method based on matching bending stiffnesses was derived to understand how to adjust the model length to represent the stiffer fillet regions between the gauge section and the grips. The suitability of this method was confirmed by performing a limited number of analyses on models that also contained the fillet and grip regions.

A series of equations was then derived to calculate the appropriate 3D FE model length as a function of the principal test piece dimensions of gauge length L_g and thickness w, grip diameter D and fillet radius r. Together with results from analyses on different length models with constrained boundary conditions, these were used to derive correction factor polynomials covering all crack lengths and all possible dimensions for this style of test piece. Geometry correction factors calculated using the polynomials were then compared with values from FE analyses run for a range of crack lengths on each of three different test piece designs.

2. Calculation procedure and results

2.1. FE modelling methods

The modelling was carried out using the ABAQUS finite element code and a series of meshes similar to that shown in Figs. 2 and 3.

The nodal co-ordinates and element definitions for the 3D mesh were generated using a Visual Basic (VB) macro in Microsoft® Excel®, together with node and element sets for the key geometric features. This approach allowed a regular mesh of the required density to be produced around the crack tip and the increase in element size away from the crack tip to be controlled.

8-noded C3D8 3D linear continuum elements were used. This approach was adopted, rather than the more conventional use of quadratic elements with collapsed corner nodes and shifted mid-side nodes [11,12] because the models will subsequently be run with creep and plasticity to model closure, crack tip blunting and crack tunnelling effects. Half the test piece was modelled, with the crack plane being the plane of symmetry. As can be seen in Fig. 2, the biasing method used to increase element size away from the crack tip can result in elements with large aspect ratios; these are, however, exclusively in regions with very low stress gradients and therefore do not influence the stresses, strains or J-integral values calculated near the crack tip. The typical number of nodes in the 3D model meshes was around 50,000.

Radial element lengths in the crack plane close to the crack tip were 2 μm for all analyses, and twenty sectors were used around the 90° crack front. To allow crack closure to be modelled (not used for the work in this paper), the mesh for a 10 μm thick rigid contact plate as shown in Fig. 3 is also generated by the VB macro.

After a number of trials, a crack tip radius of 10 μm was selected because it captures the $1/\sqrt{r}$ stress singularity at the crack tip reasonably well without generating stress magnitudes that would be difficult to converge in a non-linear run. This is demonstrated in Fig. 4 below, which compares the ln (distance)-ln (axial stress) profile from a typical elastic analysis with a straight line of gradient −0.5.

2.2. Model constraints

The first analyses run on the 3D geometry were used to check the symmetry of the stress and displacement fields between the two ends of the quarter-circular notch/crack and the correct operation of the model constraints.

All points on the model's plane of symmetry were constrained to have zero displacement in the loading (y) direction. The test piece was then further constrained in this plane at two points on its 45° diagonal. The node at the opposite corner to the crack was pinned in both x and z directions (labelled as Corner45 in Fig. 2a), and the x and (−)z displacements of the crack tip node (Crack45 in Fig. 2b) were made equal using the ABAQUS *EQUATION command.

Two sets of analyses were then run with different constraints on the loaded top face of the model. To mimic the Pickard [1] analyses a uniform pressure load was applied, allowing the top of the model to deform as it wished. Pickard's analysis work was used as a datum because his stress intensity solutions are used for analysing experimental crack growth data in the European standard for corner crack testing EN 3873 [4] and by SMaRT (Swansea Materials Research and Testing Ltd.).

The *EQUATION command was then used to link the y-direction displacements of all the nodes on the top of the model to a that of a reference node in the top corner above the crack, allowing them to move but forcing them to remain planar. This is representative of the loading conditions of the actual specimens, which are screwed into the test machine grips.

The J-integral was set up using the *CONTOUR INTEGRAL card in ABAQUS as shown below:

```
*CONTOUR INTEGRAL, crack name = Crack1, contours = 5, crack tip nodes, normal, symm
    0.0, 1.0, 0.0
    CRACKARC, TIP,
```

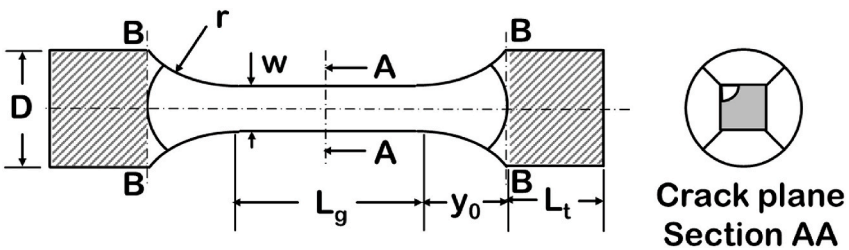

Fig. 1. Schematic corner crack test piece geometry and key dimensions (threads shown shaded).

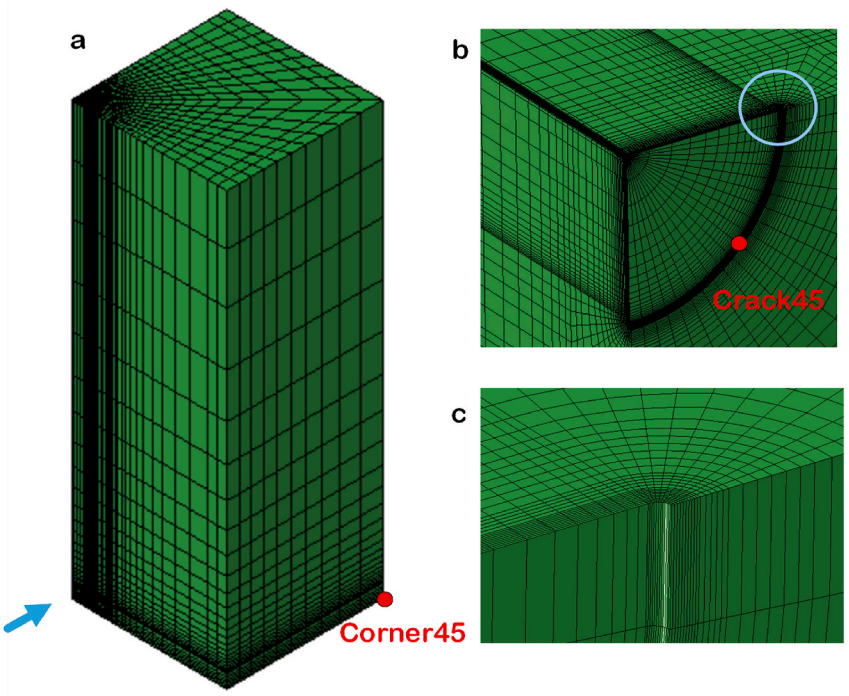

Fig. 2. Example 3D finite element model mesh: a) shows the full geometry, b) shows the view of the crack in the direction of the arrow and c) is a close-up of the circled area showing the sharp radius notch representing the crack tip.

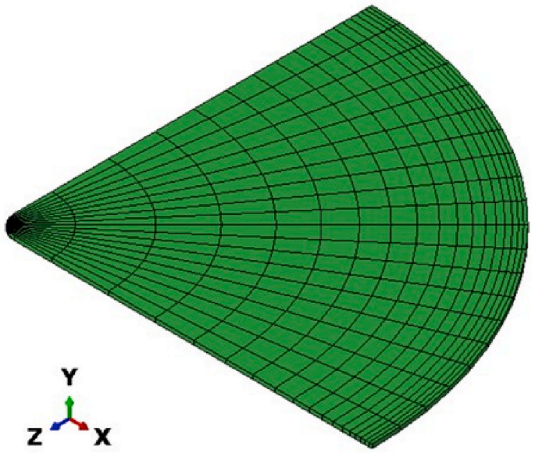

Fig. 3. 3D mesh of the contact pad used to model crack closure.

The keywords of 'contours = 5' and 'crack tip nodes' request five contour integrals around each node on the crack front and indicate that the nodes that make up the crack front will be specified. 'Normal' tells ABAQUS that the direction cosines of the normal to the crack plane will be given, and 'symm' specifies that only half the crack is modelled. In the following lines the direction cosine of the normal to the x-z propagation plane is given, and the node sets CRACKARC and TIP then indicate nodes around the crack front and the crack tip nodes.

Crack lengths of 1 mm and 4 mm in a 7 × 7mm cross-section and 17.69 mm long model with applied pressure loads of 500 and 250 MPa respectively were analysed with free and planar boundary conditions on the top face of the model. The reasons for this choice of model length will be discussed in section 2.5. Material properties for a nickel-based superalloy at 20 °C (E = 224.8 GPa, $\nu = 0.326$) were used for the runs. Non-linear geometry was used for all the analyses.

The elastic y-direction stresses from the 1 mm crack model with the planar constraint on the top surface are shown in Fig. 5. The stress contours are very smooth, and as desired the stress values at the 0 and 90° locations around the crack front are the same.

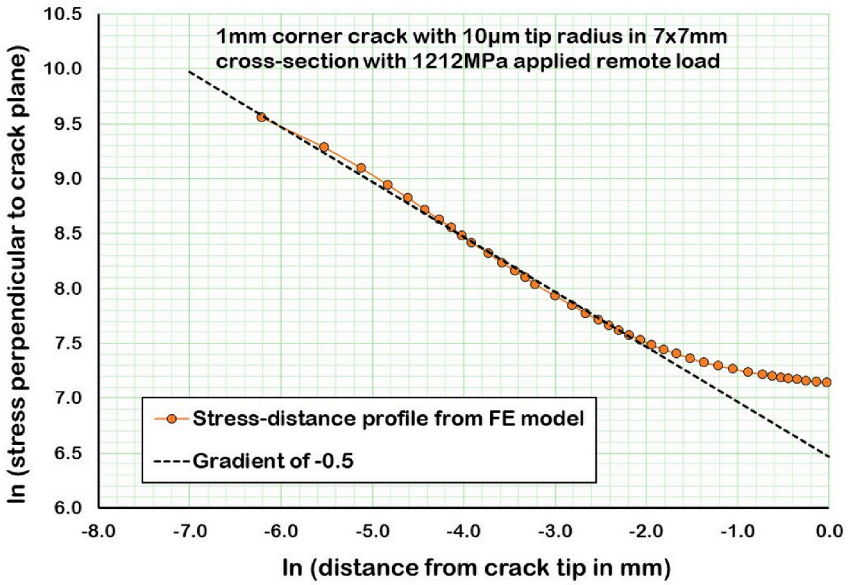

Fig. 4. Comparison of the elastic stress-distance profile ahead of the crack tip with the expected $1/\sqrt{r}$ behaviour.

The loading direction displacements calculated for the top of the 4 mm crack model with and without the planar displacement are shown in Fig. 6. The crack is at the bottom left-hand corner at the front of each of the models. As can be seen from the left-hand picture, the planar constraint on the top of the model is working correctly and the axial displacement at all the nodes is 0.23 mm. Without the planar constraint, as expected the more flexible material above the crack deforms most, with a peak value of 0.29 mm. The displacement field across the top of the model is approximately linear, and the average axial growth is very close to that of the constrained model.

2.3. *J-integral and K values*

A range of analyses for crack lengths from 0.5 to 4.5 mm with free and constrained boundary conditions was then run. The five J-integral values at each of the points around the crack fronts were extracted and converted to stress intensities and geometry correction factors using equations (1) and (2) below. Tables A1 and A2 in the Appendix show the calculated values at the surface and 45° round the crack front from these runs.

$$K = Y.\,\sigma.\,\sqrt{(\pi a)} \tag{1}$$

$$K = \sqrt{\frac{E.J}{(1-\nu^2)}} \tag{2}$$

In line with the guidance in the ABAQUS manual [13], the average J from contours 2–5 was used to calculate K. The J values show good

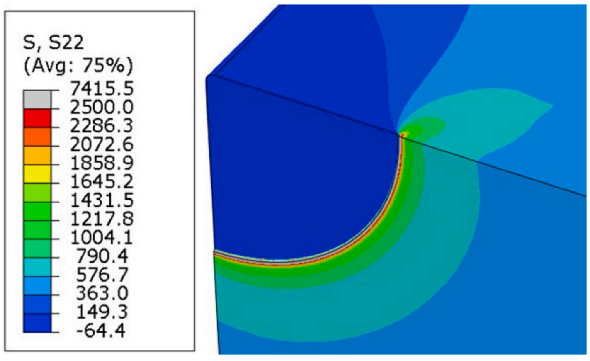

Fig. 5. y-direction elastic stresses around the crack front, 1 mm corner crack with 10 μm tip radius, 20 °C, 500 MPa applied pressure load, top surface constrained to remain planar.

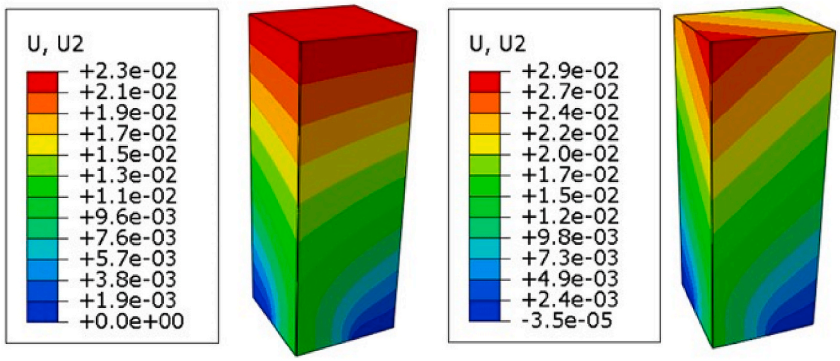

Fig. 6. Comparison of displacements on the top of the model with (left) and without (right) a planar constraint, 4 mm corner crack, 250 MPa applied pressure load.

consistency between successive contours, with those from contour 2 being slightly higher and contours 3–5 giving very similar values.

The geometry correction factor values at the 21 points around the crack tip for the analyses with the top of the model constrained are shown in a polar-type plot in Fig. 7. The variation in correction factor with position around the crack front is very smooth throughout, with the peak values being slightly sub-surface, particularly for the smaller cracks. This is consistent with results from analyses with high mesh densities such as reported by Toribio et al. [14] and Zhao et al. [15].

The FE-derived geometry correction factors are compared with the corresponding Pickard K values at the surface and 45° positions around the crack front in Figs. 8 and 9. The Pickard stress intensities were calculated using equations (3)–(10) below which were taken from Ref. [1].

$$Y = (2/\pi).M_G.M_B.M_S \tag{3}$$

where M_G, M_B and M_S are general, back face and side face correction terms that are functions of a/w, the crack length to specimen width ratio:

At the surface-breaking points on the crack, for $0 < a/w < 0.2$

$$M_G = 1.143 \tag{4}$$

$$M_B = 1 + 0.06\,(a/w) \tag{5}$$

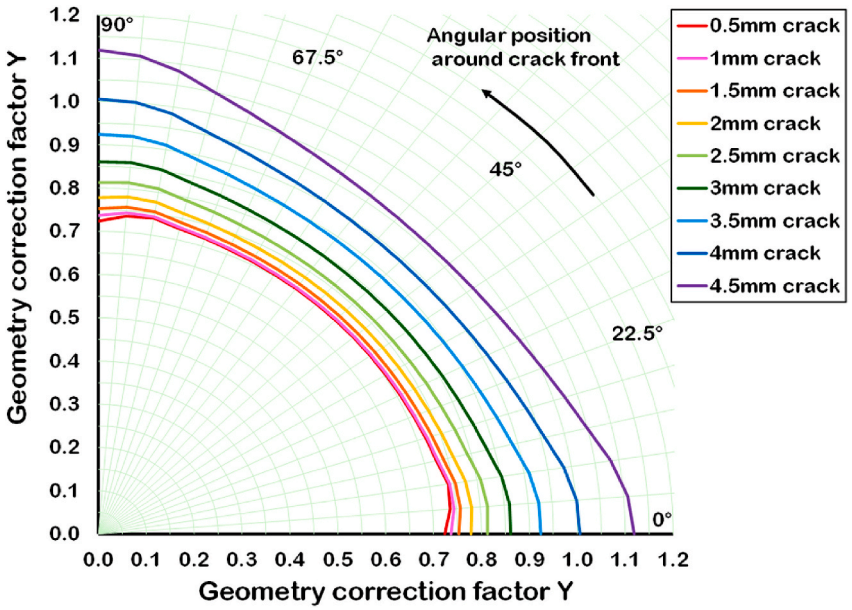

Fig. 7. Polar plot of calculated geometry correction factors for corner cracks of different lengths in the 7 × 7mm cross-section test piece, tops of FE models constrained.

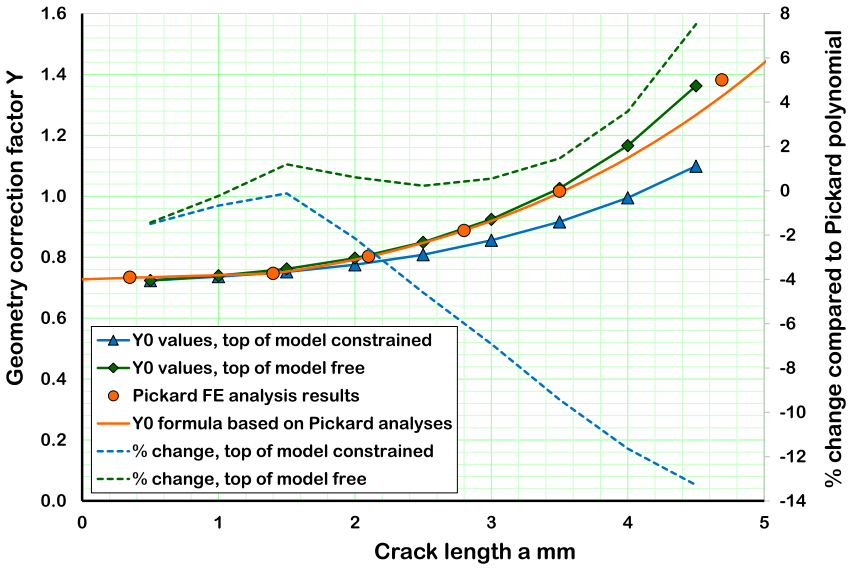

Fig. 8. Surface corner crack correction factor values from the 3D FE analyses and the Pickard equations with and without a constraint on the top of the model.

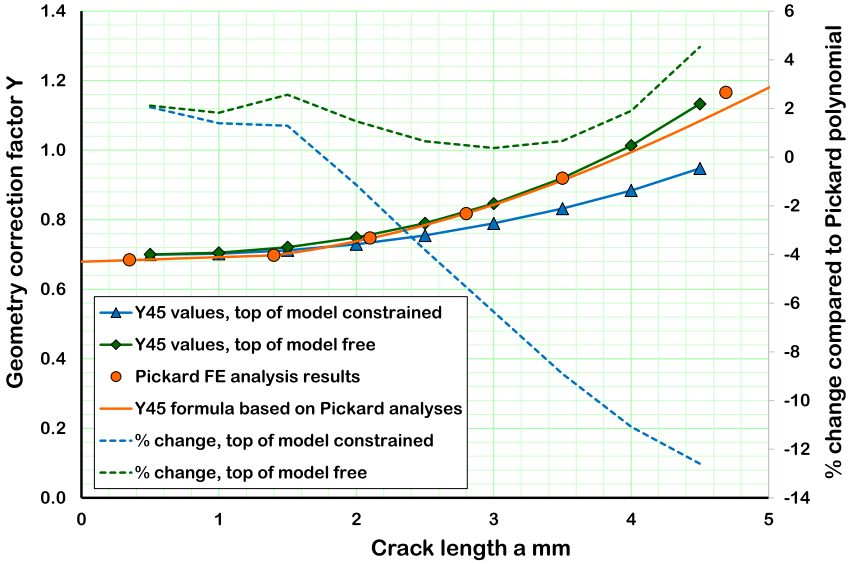

Fig. 9. 45° corner crack correction factor values from the 3D FE analyses and the Pickard equations with and without a constraint on the top of the model.

$$M_S = 1 + 0.07\,(a/w) \tag{6}$$

and for $0.2 < a/w < 0.75$

$$M_G = 1.081 + 0.29\,(a/w) + 0.1\,(a/w)^2 \tag{7}$$

$$M_B = 1.019 - 0.185\,(a/w) + 0.75\,(a/w)^2 \tag{8}$$

$$M_S = 1.02 - 0.21\,(a/w) + 0.9\,(a/w)^2 \tag{9}$$

The correction factor at the 45° point around the crack face Y45 is related to the surface correction factor Y0 by:

$$Y45 = Y0\left(0.9335 - 0.0045(a/w) + 0.1295\,(a/w)^2 - 0.4845\,(a/w)^3\right) \tag{10}$$

From both Figs. 8 and 9 it is clear that the calculated correction factors from the constrained and free models are very similar at smaller crack lengths. Here the overall displacements around the crack are relatively small, and therefore the imposed boundary conditions some distance away have virtually no effect on the stress field and the calculated correction factors. The situation is different, however, for larger cracks. The overall displacements close to the crack tip are now greater, and the effect of constraining the model is to introduce additional compression above the corner containing the crack, reducing the J, K and Y values compared to the unconstrained models.

At both locations around the crack, the correction factors from the 3D model with a free top surface agree very well with Pickard's values, particularly his FE analysis results, up to a crack length of around 3.5 mm. Above this, however, the results from this study are slightly higher. The reasons for this are not clear, although the greater mesh density in this work may give more accurate results when the crack tip displacements are high. A sensitivity study for three crack lengths using linear geometry and both constrained and free boundary conditions gave geometry correction factors that were slightly higher but always within 0.5% of those using non-linear geometry, and this was therefore ruled out as a potential source of the discrepancy between the results in this study and Pickard's.

The dashed lines in Figs. 8 and 9 show the percentage difference between the K values from the 3D analyses and the Pickard polynomial. The kinks at 1.4 mm are caused by there being two sets of Pickard coefficients for small and large cracks. As expected, the differences for the analyses with the top of the model free to deform are small, within 3% for crack lengths up to 3.5 mm, but above that they increase rapidly to peaks of 7.5% (on the surface) and 4.5% (at the 45° position) at 4.5 mm.

At the surface location shown in Fig. 8, the divergence between the results from models with the top constrained and free starts at around 1.5 mm, with the FE correction factor for a 4.5 mm crack with a top constraint being 13.3% lower than the Pickard value for a 4.5 mm long crack.

Similar trends can be seen in the corresponding plot for the 45° location in Fig. 9, with the maximum difference between the 3D model results with the top constrained and the Pickard polynomial being 12.6%.

As a check on the sensitivity of the correction factor values to the material properties used, the 4 mm crack analysis with constrained boundary conditions was re-run with a modulus of 100 GPa and a Poisson's ratio of 0.333 to represent a generic Ti-based alloy. The geometry correction factors at the surface and 45° crack locations were 0.4% lower and 0.1% higher respectively than from the original analysis for a Ni-based alloy (E = 224.8 GPa, $\nu = 0.326$), indicating that they are largely insensitive to the mechanical property values used in the FE analyses.

2.4. *Effects of 3D model length on the calculated correction factors*

To understand the effects of the length of the 3D model on the calculated geometry correction factors, a sensitivity study was performed using a 4.5 mm crack length. Analyses with and without the top of the model constrained were run on models with the same crack tip mesh but with different half-lengths equally spaced on a log (length) axis. Five model half-lengths were run, a datum of 18 mm and four representing factors of $1/2$, $1/\sqrt{2}$, $\sqrt{2}$ and 2 on this length. The results are shown in Fig. 10 and Table A3.

With the top of the model free to deform, the axial length has no effect on the correction factor values anywhere around the crack front for models longer than 9 mm. This is in line with previously reported trends [16]: at locations away from the immediate vicinity

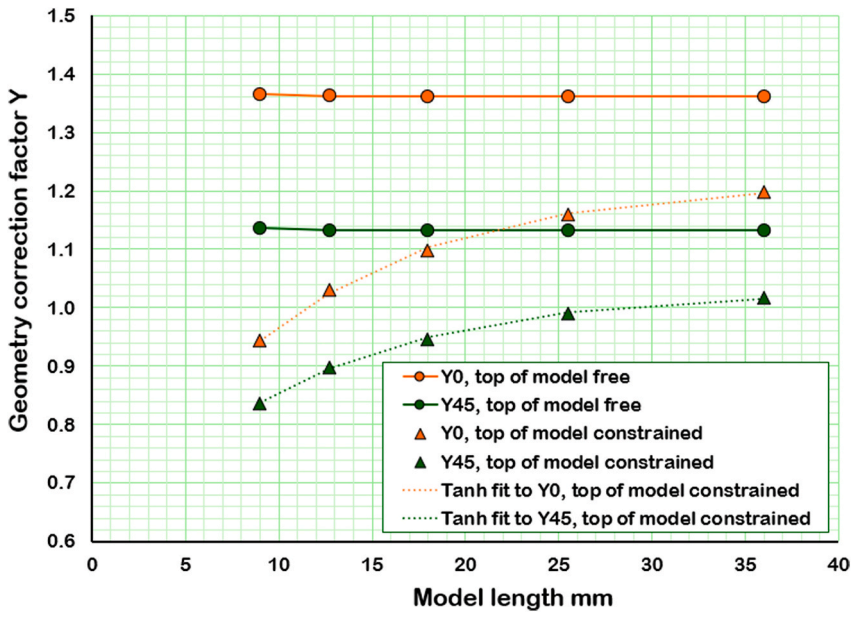

Fig. 10. Effects of model axial length on the calculated correction factors for a 4.5 mm corner crack in a 7 × 7mm section, top of FE models constrained.

of the crack the stress field will almost be purely axial, and the addition of extra material will not change the state of stress or the deformations closer to the crack plane. The 9 mm model is slightly too short for the deformations around the crack tip to be constrained in the same way as the other models, resulting in marginally higher correction factors around the crack front. An additional unconstrained run with a model length of 4.5 mm produced even more deformation of the unsupported material above the crack face and an increase in correction factors around the crack front.

When the top of the model is constrained, the reduction in geometry correction factor compared to the free model depends on how the crack tip region displaces in the different length models. For long models, sections close to the crack tip with the same initial axial co-ordinates will still have higher displacements at the corner containing the crack. As the model length is reduced, the imposition of a planar constraint closer to these sections limits the variation in displacement across them, increasing the compression generated by the constraint and hence reducing the crack tip correction factor values. Note that even for very long models the constraint still has the effect of introducing a bending moment that helps to close the crack, and hence the constrained geometry correction factors will always be smaller than those for a model with the top free.

The variation in correction factor with 3D model length L_{3D} in Fig. 10 was represented by a hyperbolic tangent function as shown below in equations (11) and (12).

Where the crack meets the test piece faces

$$Y_{L\,0} = \alpha_0 \tanh(\beta_0\,(L_{3D} - L_0)) \tag{11}$$

and at the 45° location around the crack tip

$$Y_{L\,45} = \alpha_{45} \tanh(\beta_{45}\,(L_{3D} - L_{45})) \tag{12}$$

where $Y_{L\,x}$ is the geometry correction factor as a function of model length and α_x, β_x and L_x are fitting parameters determined using the least squares method. The optimised values of these parameters are shown in Table 1 and were used to generate the dotted lines in Fig. 10. As also shown in Table 1, the correction factors calculated from the equations were all within 0.4% of the values from the 3D FE analyses.

2.5. Appropriate 3D model lengths

The 3D models used for the FE analyses above have a square cross-section of constant dimensions along their lengths, unlike the test piece which gets thicker towards the grips. In order to compensate for this, their axial length was chosen to produce a bending stiffness similar to that of the test piece. This was done by equating the theoretical deflections of the uncracked test piece under a perpendicular load at its mid-point and a constant section beam whose length was varied.

For the test piece, the centrally applied load P in Fig. 11 generates equal reactions of $P/2$ and bending moments of magnitude M_G at the built-in ends. The figure also shows the shear force and bending moment diagrams for the system. It is assumed that all points on the planes at the junctions between the fillet and threaded regions of the test piece (BB in Fig. 1) have the same axial displacements.

If the vertical deflection of the beam is δ at any axial distance x along the beam, basic beam bending theory as discussed in Crandall, Dahl and Lardner [17] states that

$$\text{Beam curvature } \frac{d^2\delta}{dx^2} = \frac{M(x)}{EI} \tag{13}$$

$$\text{Slope } \frac{d\delta}{dx} = \int \frac{M(x)}{EI}\,dx \tag{14}$$

$$\text{Deflection } \delta = \int \left(\int \frac{M(x)}{EI}\,dx \right) dx \tag{15}$$

where $M(x)$ is the bending moment as a function of axial distance, E is Young's modulus and I is the moment of area, equal to (depth)^4/12 for a beam with a square cross-section.

The depth d of the radiused part of the test piece at a distance x from the grip is

Table 1
Parameters describing the variation in constrained geometry correction factors with 3D model length.

Optimised parameter values:	Alpha0	1.213		Alpha45	1.028	
	Beta0	0.0534		Beta45	0.0525	
	L0	−10.50		L45	−12.76	
Model length L mm	Y0 from FE	Y0 from equation	% difference	Y45 from FE	Y45 from equation	% difference
9.0	0.943	0.945	−0.19	0.837	0.839	−0.14
12.7	1.029	1.026	0.35	0.898	0.896	0.27
18.0	1.102	1.103	−0.07	0.950	0.950	−0.06
25.5	1.159	1.162	−0.25	0.990	0.992	−0.20
36.0	1.198	1.196	0.16	1.017	1.016	0.13

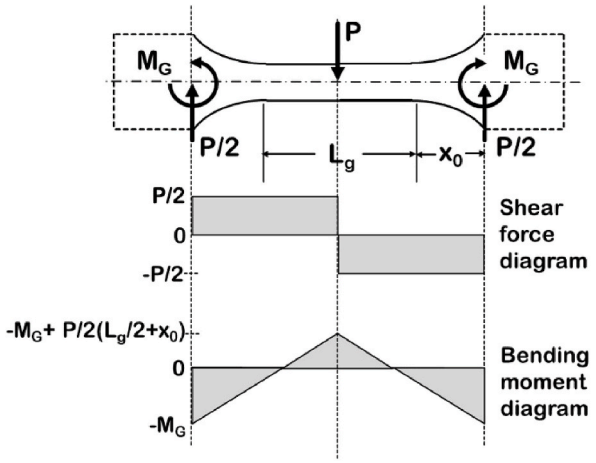

Fig. 11. Test piece shear force and bending moment diagrams.

$$d = \mathrm{w} + 2\left(r - \sqrt{r^2 - (x - x_0)^2}\right) \tag{16}$$

This variation in depth with distance means that 1/I cannot be integrated analytically, and therefore a spreadsheet was used to integrate *M(x)* over the half-length of the test piece in 0.01 mm increments.

The bending moments M_G at the test piece grips cannot be determined by resolving forces and moments, but in order for the slope of the test piece at the grips and its centre to be zero their value must be such that the area under the *M(x)/I* curve is zero. In the spreadsheet, therefore, the Solver add-in was used to determine the value of M_G that satisfied this condition. The constants *P* and *E* were not included in the spreadsheet calculations because these will cancel out between the calculations for the test piece and the constant section square bar.

The spreadsheet was then used to sum the slope increments over the half length of the test piece to generate deflections. Example results for a test piece and a constant section beam (simulated by setting the grip diameter *D* equal to the gauge width *w*) are shown in Fig. 12. In order to check the correct operation of the spreadsheet, the central deflection of the constant section beam was compared with the standard solution quoted in Howatson, Lund and Todd [18]. The deflection agreed extremely closely with the expected value of $PL^3/192EI$, where *L* is the length of the uniform beam.

As a comment on the above calculations, the key direction in which the bending stiffnesses should be matched between the actual test pieces and the 3D constant section models is about an axis between diagonally opposite corners on the test piece's cross-section rather than the minimum stiffness direction considered above. The approach adopted for matching the stiffnesses is considered

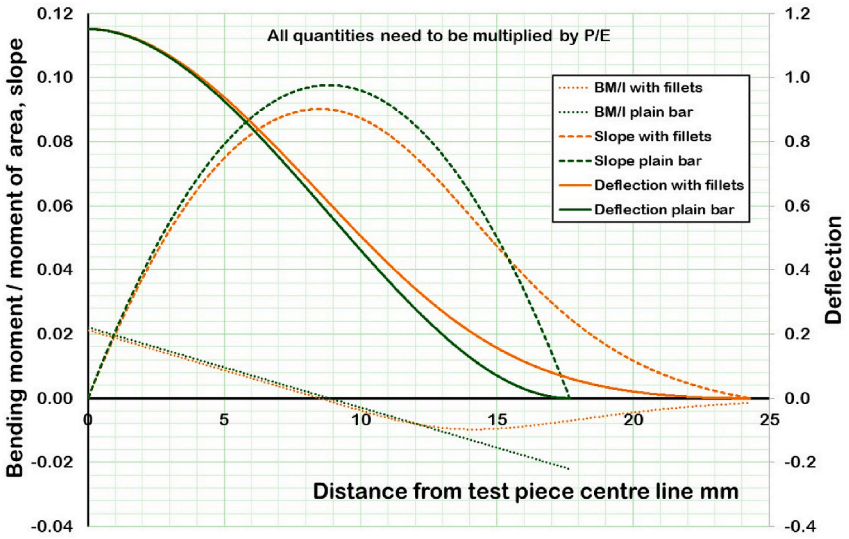

Fig. 12. Bending moment/moment of area, slope and deflection calculations for a test piece with fillet radii and the equivalent stiffness constant section beam.

appropriate, however, because bending about the diagonal axis can be considered as the superposition of a bending moment about one of the minimum stiffness directions followed by an equal moment about the other.

In order to be able to generate equivalent lengths for any similar test piece design, the spreadsheet described above was run with multiple values for fillet radius, grip diameter and parallel gauge length. Runs were also undertaken to confirm that multiplying these parameters and the section thickness w by a constant scaling factor produced equivalent 3D model lengths that were scaled by the same constant.

The equivalent axial lengths of the fillet regions calculated for a wide range of different input dimensions, normalised by the section width w, are shown in Figs. 13–15 below as a function of the parallel gauge section length, grip diameter and fillet radius respectively. A gauge section width of 5 mm was used throughout, but its actual value is not important because of the normalisation process. Different curve forms were then proposed to represent the observed shapes of these relationships as shown below:

$$L_{eq\ rad} = O_1 . f\left(\frac{L_g}{w}\right) . g\left(\frac{r}{w}\right) . h\left(\frac{D}{w}\right) \tag{17}$$

where

$$f\left(\frac{L_g}{w}\right) = l_0 - l_1 \exp\left(l_2 \left(\frac{L_g}{w} - l_3\right)\right) \tag{18}$$

$$g\left(\frac{r}{w}\right) = r_0 \left(\frac{r}{w} - r_1 \frac{D}{w}\right)^{r_2} \tag{19}$$

$$h\left(\frac{D}{w}\right) = d_0 + \frac{d_1}{\left(\frac{D}{w} - d_2\right)} \tag{20}$$

The values of the eleven subscripted coefficients were then determined using least squares methods and the Excel Solver add-in. The fitted curves generated using these coefficients are shown alongside the input data points in Figs. 13–15. The overall accuracy of the fit is very good, with the maximum discrepancy between actual and predicted values being less than 0.02w. The coefficient values are shown below in Table 2.

Using equations 17–20, the equivalent 3D model length to represent the datum corner crack test piece used by Swansea University ($w = 7$ mm, $L_g/2 = 10$ mm, $r = 25$ mm, $D = 16$ mm and $L_t = 18$ mm in Fig. 1) is 17.69 mm, hence its use for all the analyses described to date. Because all points on planes BB are assumed to have the same axial displacements, the length of the threaded regions L_t does not affect the calculations. In practice, this assumption is justified because the threads are usually long compared to the grip diameter.

To verify the appropriateness of the equivalent stiffness method used to determine the 3D model length, a number of J-integral calculations were also made on a half model of the datum 7 × 7mm cross-section test piece that included the grip regions. The model and a plot showing axial displacements for an applied pressure load of 500 MPa on a 2.5 mm long crack are shown in Fig. 16.

Crack lengths of 1, 2.5 and 4 mm were analysed with both free and constrained boundary conditions in the grip region. The mesh for the first 5 mm axially from the crack plane was generated using Excel, as before. This was fully tied to a C3D10 tetrahedral mesh of

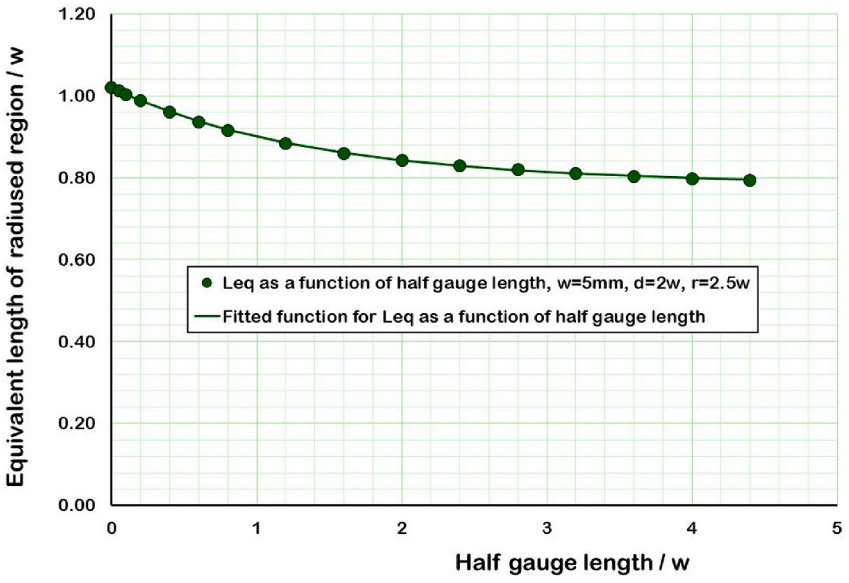

Fig. 13. Variation in equivalent axial length of test piece radiused regions as a function of parallel gauge section length/w.

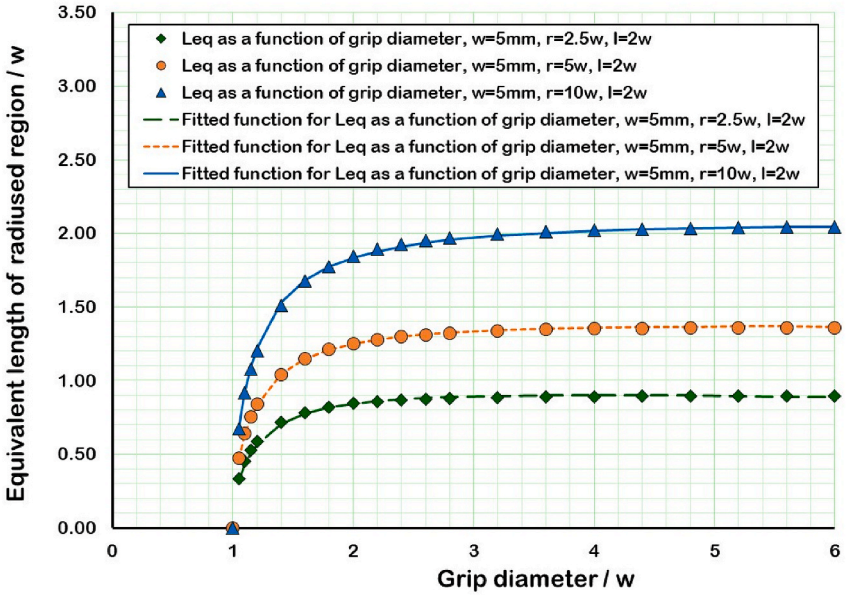

Fig. 14. Variation in equivalent axial length of test piece radiused regions as a function of grip diameter/w.

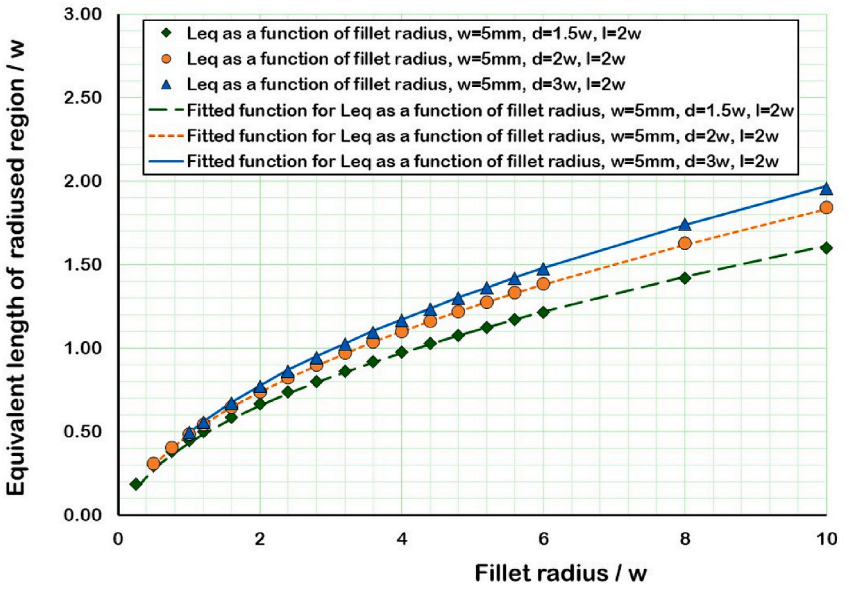

Fig. 15. Variation in equivalent axial length of test piece radiused regions as a function of fillet radius/w.

Table 2
Fitted coefficients describing the equivalent axial length of the test piece fillet regions as a function of parallel gauge section length, grip diameter and fillet radius.

Diameter terms	d0	0.273	Length terms	l0	1.300
	d1	−0.0482		l1	−0.348
	d2	0.791		l2	−0.709
	r0	1.105		l3	0.142
Radius terms	r1	0.0726	Overall factor	O1	1.474
	r2	0.544			

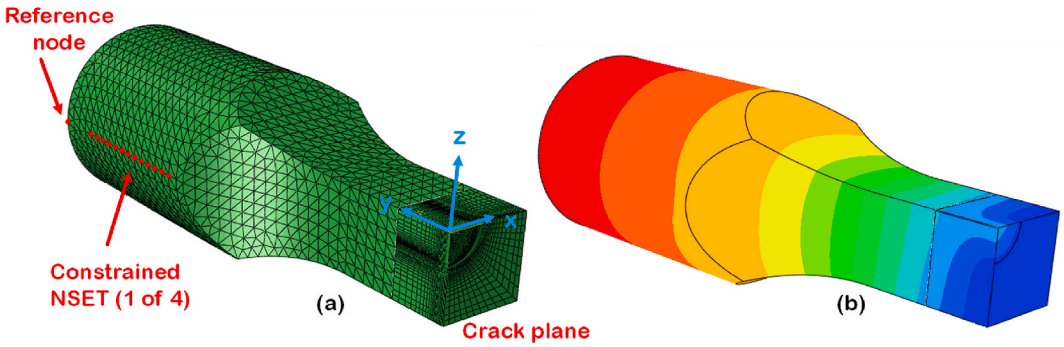

Fig. 16. Full test piece model: Mesh (a) and contours of axial displacement under load (b).

the rest of the test piece produced in ABAQUS CAE. For the constrained models, all nodes on the loaded end face were made to have the same axial displacements as a reference node in the centre by using the *EQUATION ABAQUS keyword. The built-in conditions imposed by the test piece threads were represented by forcing four series of nodes at the 3, 6, 9 and 12 o'clock positions around the threads to have the same x-z plane displacements as reference nodes on the circumference of the end face of the model. This arrangement, also using *EQUATION, is shown in Fig. 16a for the 9 o'clock series of nodes (as viewed from the crack plane). The original x and z co-ordinates are the same for the nodes in the NSET and the reference node, and the applied constraint keeps those four sets of nodes in vertical lines, mimicking the behaviour of the test piece grips. For the free boundary conditions, no constraints were applied in the grip region or to the loaded end of the test piece.

The geometry correction factors calculated for constrained boundary conditions using full test piece models are shown alongside those from constant cross-section models in Fig. 17. The calculated correction factors from the two methods are also compared in Table 3.

The calculated geometry correction factors from the full and constant cross-section models for the three crack lengths with both constrained and free boundary conditions agree very closely, with a maximum difference of 0.4%. For all conditions, including the grip regions in the models reduces the correction factors very slightly.

The similarity between the constrained boundary condition results for the full and constant cross-section models strongly supports the use of the equivalent stiffness method for determining an appropriate length for the constant cross-section models. This will allow geometry correction factor polynomials to be calculated relatively easily for all corner crack test pieces of the style shown in Fig. 1, whatever their dimensions.

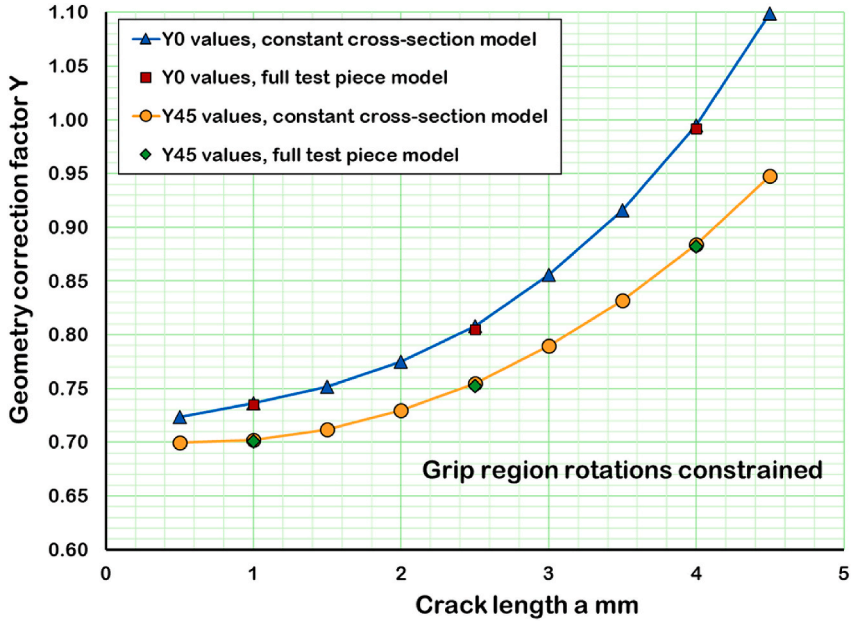

Fig. 17. Geometry correction factors from full test piece models and constant cross-section models whose lengths were determined using the equivalent bending stiffness method.

Table 3
Comparison of geometry correction factors calculated using the full and constant cross-section test piece models.

Crack length mm	Constrained boundary conditions						Free boundary conditions					
	Y0			Y45			Y0			Y45		
	Full model	Constant x-section	% difference	Full model	Constant x-section	% difference	Full model	Constant x-section	% difference	Full model	Constant x-section	% difference
1	0.735	0.736	0.14	0.701	0.702	0.14	0.738	0.740	0.27	0.704	0.705	0.14
2.5	0.805	0.808	0.37	0.752	0.755	0.40	0.846	0.849	0.35	0.787	0.790	0.38
4	0.992	0.995	0.30	0.882	0.884	0.23	1.163	1.167	0.34	1.010	1.013	0.30

2.6. FE analyses for other test piece geometries

The appropriate equivalent 3D model half-lengths for two other corner crack test pieces used by Swansea University with the dimensions shown in Table 4 were then calculated using equations 17–20. Test pieces A (the 7 × 7mm cross-section datum) and B have similar overall dimensions apart from the gauge section width. Test piece B is thicker, making the ratio between its equivalent 3D model length and width lower than for specimen A. This should make its constrained geometry correction factors for a given a/w lower than for the 7 × 7mm test piece A. In contrast, the 5 × 5mm cross-section test piece C has a longer parallel gauge region than the other two specimens and a higher equivalent model length to width ratio. Its calculated correction factors for a given a/w with constrained boundary conditions are therefore expected to be the highest.

ABAQUS 3D models with both free and constrained boundary conditions were then constructed for test pieces B and C using the Excel spreadsheet described earlier. Thirteen crack lengths from 0.5 to 6.5 mm in 0.5 mm increments were analysed for the 10 × 10mm cross-section test piece B, and seven crack lengths from 0.5 to 3.5 mm were analysed for test piece C. The J-integral, K and geometry correction factor values at the surface and 45° positions around the crack front from these analyses are shown in Tables A4-A7.

3. Discussion

3.1. Correction factor polynomials for unconstrained boundary conditions

The calculated correction factor values at the surface and 45° locations around the crack front from the unconstrained 3D FE analyses for all three test piece designs are shown in Figs. 18 and 19. The crack lengths a were normalised by the section width w.

As can be seen, the data points collapse well and can be represented by polynomial expressions in a/w. Polynomials with even number powers of a/w were used because of the shape of the Y vs. crack length curves, and the data fitting was performed using the Solver function in Excel. The match between the solid lines from the polynomials and the individual model results shown as points is excellent, with the polynomial-derived values always being within 1% of the FE model results. An overall factor of $2/\pi$ was included to be consistent with the convention for circular crack correction factor polynomials and to produce coefficients with values closer to unity. One expression at each crack front location was found to be adequate to cover the full range of practical crack sizes in the test pieces rather than having two sets of coefficients for a/w values either side of 0.2 as with the Pickard polynomials.

$$Y_{x\ FREE} = \frac{2}{\pi}\left(a_{0x} + a_{2x}\left(\frac{a}{w}\right)^2 + a_{4x}\left(\frac{a}{w}\right)^4\right) \tag{21}$$

Including the values of the fitted coefficients, this becomes

$$Y_{0\ FREE} = \frac{2}{\pi}\left(1.139 + 1.058\left(\frac{a}{w}\right)^2 + 3.332\left(\frac{a}{w}\right)^4\right) \tag{22}$$

$$Y_{45\ FREE} = \frac{2}{\pi}\left(1.087 + 1.008\left(\frac{a}{w}\right)^2 + 1.627\left(\frac{a}{w}\right)^4\right) \tag{23}$$

3.2. Correction factor polynomials for constrained boundary conditions

Under constrained boundary conditions, because the geometry correction factor depends on model length and the gauge lengths, fillet radii and grip diameters of the three test pieces are not in proportion the results at a specific crack location do not collapse onto a unique curve. The symbols in Figs. 20 and 21 show the calculated correction factors as a function of a/w.

In an attempt to derive a correction factor expression that works for all three geometries, the model lengths for test pieces B and C were first scaled on the width ratio between them and the 7 × 7mm section test piece A. This takes advantage of the geometric scaling possible with crack tip stress fields and allows the information on how length affects correction factors from Fig. 10 to be used for the other test piece geometries.

The equivalent model length L_{EQ3D} after scaling to a test piece width of 7 mm is defined as

$$L_{EQ3D} = L_{3D}\ \frac{w_{datum}}{w_{act}} \tag{24}$$

where w_{datum} is the width of the datum model (=7 mm) and w_{act} is the width of the 3D model.

Using equation (24), the equivalent length of the 18.3 mm long test piece B models at a section width of 7 mm is 12.8 mm. The

Table 4
Dimensions of test pieces used at Swansea University and calculated equivalent 3D model lengths.

Test piece	Gauge section width mm	Gauge length mm	Fillet radius mm	Grip diameter mm	Equivalent 3D model half length mm
A	7	10	25	16	17.69
B	10	10	25	16	18.30
C	5	12.5	12.7	11	16.75

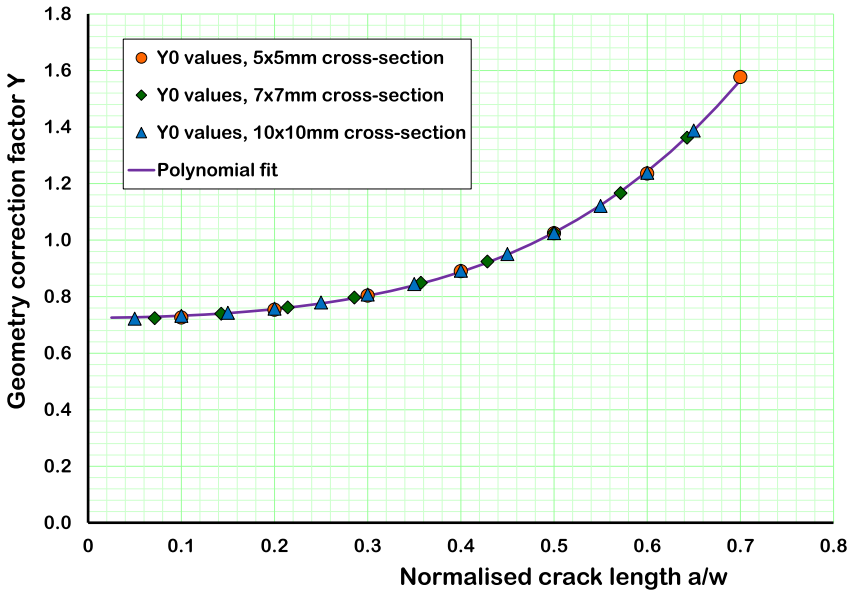

Fig. 18. Comparison between the FE-derived corner crack surface correction factor values (symbols) and the fitted polynomial (solid line) for free boundary conditions.

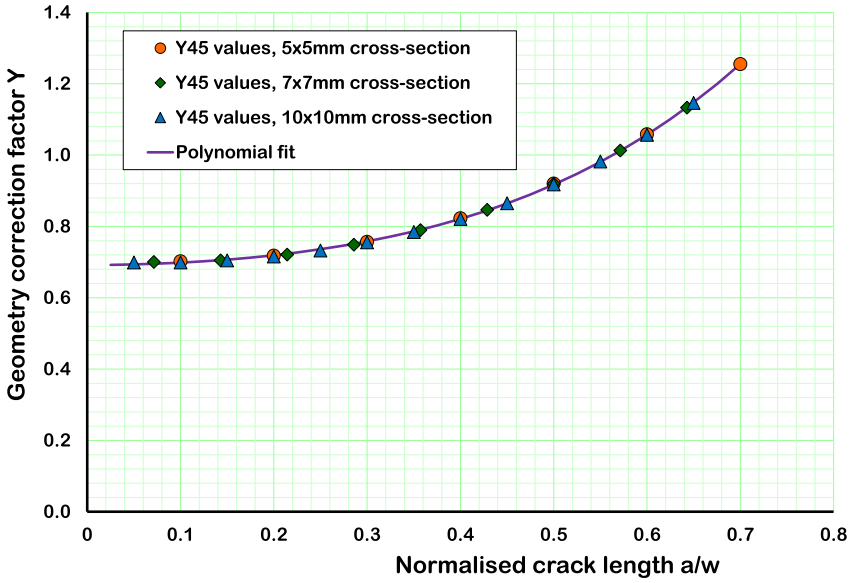

Fig. 19. Comparison between the FE-derived corner crack 45° correction factor values (symbols) and the fitted polynomials (solid lines) for free boundary conditions.

corresponding value for the test piece C models is 23.5 mm.

A model length-dependent term was added to the geometry correction factor polynomial of equation (21) to make it applicable to constrained boundary conditions. At very small crack lengths, however, the correction factors are independent of the model length and whether its top boundary is free or constrained. The relevant values of a_{0x} were therefore read across from the unconstrained polynomial fits of equations (22) and (23), and the model length factor Y_{LFACx} was applied to just the a/w polynomial terms as shown below in equation (25).

$$Y_{x\ FIXED} = \frac{2}{\pi}\left(a_{0x} + Y_{LFACx}a_{2x}\left(\frac{a}{w}\right)^2 + Y_{LFACx}a_{4x}\left(\frac{a}{w}\right)^4\right) \tag{25}$$

The datum model length used when calculating Y_{LFACx} is 17.69 mm, the length of the 7 × 7mm cross-section FE models used in the

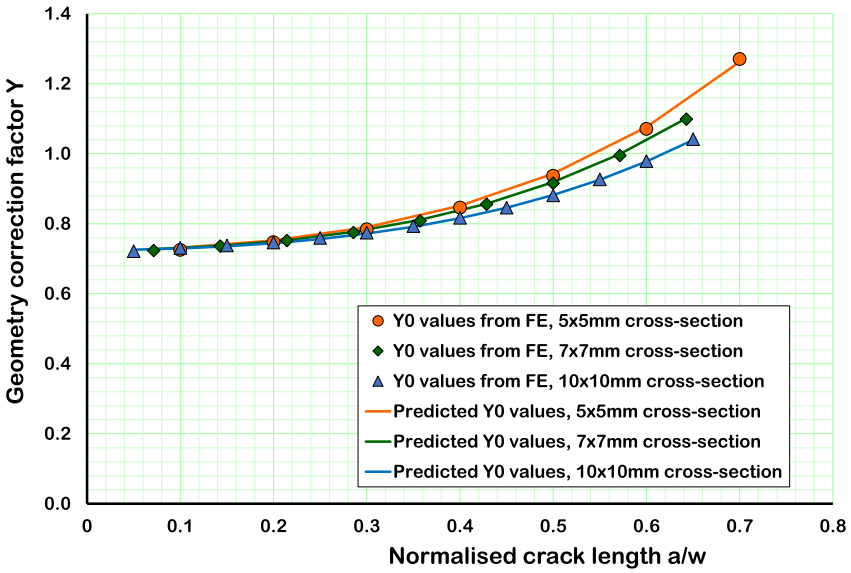

Fig. 20. Comparison between the FE-derived corner crack surface correction factor values (symbols) and fitted polynomials (solid lines) for constrained boundary conditions.

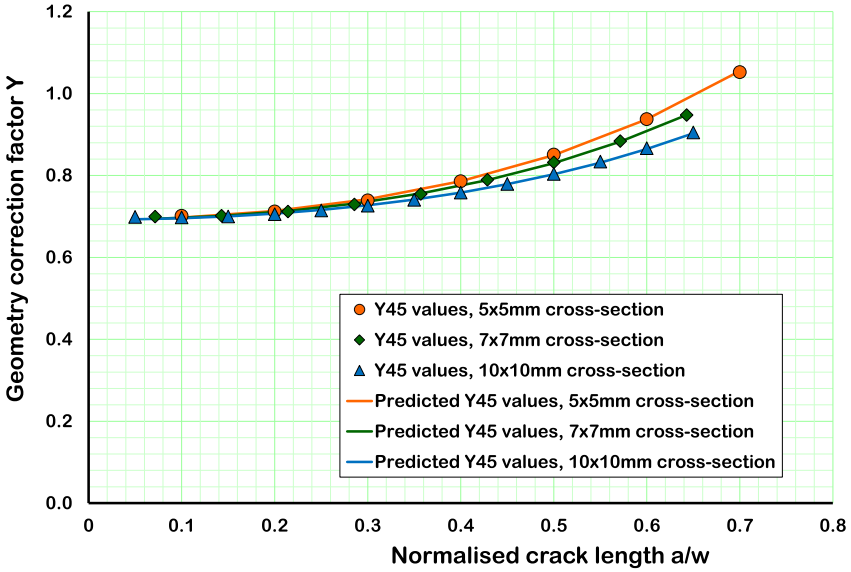

Fig. 21. Comparison between the FE-derived corner crack 45° correction factor values (symbols) and fitted polynomials (solid lines) for constrained boundary conditions.

correction factor calculations. Y_{LFACx} at this length is assumed to be 1, and therefore the a_{2x} and a_{4x} terms can be fitted to the correction factor results at different crack lengths from this test piece.

Their optimised values, determined using least squares methods and the Excel Solver add-in, are given in Table 5.

Combining equations (11), (12) and (25) at the a/w value of (4.5/7) = 0.643 used for the model length sensitivity study gives the

Table 5
Coefficients fitted to the correction factor results from the 7 × 7mm cross-section test pieces, constrained boundary conditions.

$a_{0\,0}$	1.139	$a_{0\,45}$	1.087
$a_{2\,0}$	0.893	$a_{2\,45}$	0.711
$a_{4\,0}$	1.292	$a_{4\,45}$	0.639

relationship between Y_{LFACx} and equivalent 3D model length L_{EQ3D} shown in equations (26) and (27):

$$\frac{2}{\pi}\left(a_{0x} + Y_{LFACx}a_{2x}\left(\frac{a}{w}\right)^2 + Y_{LFACx}a_{4x}\left(\frac{a}{w}\right)^4\right) = \alpha_x \tanh((\beta_x\,(L_{3D} - L_x)) \tag{26}$$

$$Y_{LFACx} = \frac{\left(\frac{\pi}{2}\alpha_x \tanh(\beta_x\,(L_{EQ3D} - L_x)\right) - a_{0x}\right)}{\left(a_{2x}\left(\frac{a}{w}\right)^2 + a_{4x}\left(\frac{a}{w}\right)^4\right)} \tag{27}$$

Note that because different fitting errors exist in both the numerator and denominator of equation (27) the values of Y_{LFACx} for the datum 7 × 7mm cross-section test piece A are not 1 but 1.003 and 0.997 respectively for Y_{LFAC0} and Y_{LFAC45}. These small inaccuracies when calculating the correction factor polynomials are considered to be acceptable given that the equivalent 3D model length and hence Y_{LFACx} and the correction factor polynomials can now be calculated for any geometry similar to that of the test pieces analysed here.

Substituting the values of the relevant coefficients from Tables 5 and 11 into equation (27) gives the following simplified equation forms:

$$Y_{LFAC0} = 3.253 \tanh(0.0534\,(L_{EQ3D} + 10.5)) - 1.945 \tag{28}$$

$$Y_{LFAC45} = 4.008 \tanh(0.0525\,(L_{EQ3D} + 12.76)) - 2.697 \tag{29}$$

Although equation (25) will give good quality correction factor values at an a/w of 0.643, the value used for the length sensitivity studies, its accuracy at other crack lengths still needs to be established. Accordingly, constrained boundary condition correction factor values for the three test piece designs were predicted using equations (24), (25), (28) and (29) and compared with the FE results from Tables A2, A6 and A7 as shown in Table A8 and Figs. 20 and 21.

The quality of the fit is extremely good, with all the errors between the geometry correction factor values calculated from the equations and those from the FE models being below 1%.

4. Conclusions

The analyses reported in this paper demonstrate the importance of modelling the constraints correctly when predicting geometry correction factor values for corner crack test pieces.

Although the FE methods used are slightly unconventional, the correction factor values obtained from unconstrained analyses agree very closely with those from Pickard's work [1] for all but the highest crack lengths.

With a planar constraint applied to represent test piece behaviour more correctly, the correction factor values reduce. The magnitude of this reduction is related to the crack length and the test piece geometry, particularly the ratio of its axial length to its width: shorter test pieces for a given width have lower constrained correction factors. For the 7 × 7mm cross-section test piece geometry used at Swansea University, constrained correction factors at the highest experimental crack lengths are around 20% lower than unconstrained correction factors.

Associating experimentally measured crack growth rates with unconstrained correction factors will over-estimate K values and make the material appear to be stronger than reality. It is therefore recommended that the constrained geometry correction factors from this paper are used to analyse laboratory test results and generate materials property data. Because the constrained and unconstrained correction factors are very similar at smaller crack lengths, however, the effects on component lifetimes of using growth rate data analysed using unconstrained correction factors will be limited (typically a 5% over-estimate).

Based on matching the bending stiffnesses of built-in beams with a central point load, methods were developed for determining appropriate 3D FE model lengths to represent specific test piece geometries. These were generalised through a series of equations that allow constrained correction factor polynomials to be obtained directly for all corner crack test piece geometries of the same style as used in this study.

Values from these polynomials agree extremely well with values from the FE analyses, within 1% for a wide range of crack lengths on three different test piece designs.

Author statement

All the work described in the paper was carried out by me, as was its preparation. I have received minor assistance along the way from colleagues at Swansea University and my PhD supervisor, but all parties have agreed that this was not of sufficient significance to warrant their inclusion on the author list.

Declaration of competing interest

The authors declare the following financial interests/personal relationships which may be considered as potential competing interests: Stephen Williams reports financial support and equipment, drugs, or supplies were provided by Rolls-Royce plc. Stephen Williams reports a relationship with Rolls-Royce plc that includes: employment and equity or stocks.

Data availability

Data will be made available on request.

Acknowledgements

The author is grateful for the financial support provided for this work by Rolls-Royce plc. The work was carried out at the Institute of Structural Materials in Swansea University as part of a Ph.D. project.

8 Appendix.

Results tables from Finite Element analyses.

Table A1
Corner crack geometry correction factor calculations for different crack lengths from the 3D FE analyses at the surface and 45° locations around the crack front, top of model free to deform, 7 × 7mm cross-section models

Crack length mm	a/w	Applied load MPa	Angle deg	J-integral values for contour no. MPa.mm					Av. J2-J5 MPa.mm	E GPa	Poisson's ratio	K MPa$\sqrt{m}$	Y	Y Pickard
				J1	J2	J3	J4	J5						
0.5	0.07	500	0	0.821	0.818	0.818	0.818	0.819	0.818	224.8	0.326	14.35	0.724	0.734
1	0.14	500	0	1.715	1.709	1.707	1.707	1.708	1.708	224.8	0.326	20.72	0.740	0.741
1.5	0.21	500	0	2.732	2.721	2.718	2.717	2.718	2.719	224.8	0.326	26.15	0.762	0.753
2	0.29	500	0	3.988	3.972	3.967	3.965	3.965	3.967	224.8	0.326	31.59	0.797	0.792
2.5	0.36	500	0	5.657	5.634	5.626	5.623	5.623	5.627	224.8	0.326	37.62	0.849	0.847
3	0.43	250	0	2.012	2.004	2.001	2.000	2.000	2.001	224.8	0.326	22.44	0.924	0.919
3.5	0.50	250	0	2.893	2.881	2.877	2.876	2.875	2.877	224.8	0.326	26.90	1.026	1.011
4	0.57	250	0	4.273	4.256	4.249	4.247	4.246	4.250	224.8	0.326	32.69	1.167	1.126
4.5	0.64	250	0	6.557	6.531	6.521	6.517	6.516	6.521	224.8	0.326	40.50	1.362	1.267
0.5	0.07	500	45	0.770	0.767	0.766	0.765	0.765	0.766	224.8	0.326	13.88	0.700	0.686
1	0.14	500	45	1.562	1.555	1.552	1.551	1.550	1.552	224.8	0.326	19.76	0.705	0.692
1.5	0.21	500	45	2.449	2.439	2.435	2.433	2.432	2.435	224.8	0.326	24.75	0.721	0.703
2	0.29	500	45	3.523	3.508	3.502	3.499	3.498	3.502	224.8	0.326	29.68	0.749	0.738
2.5	0.36	500	45	4.899	4.879	4.870	4.866	4.864	4.870	224.8	0.326	35.00	0.790	0.785
3	0.43	250	45	1.688	1.681	1.678	1.676	1.676	1.678	224.8	0.326	20.54	0.846	0.843
3.5	0.50	250	45	2.323	2.314	2.310	2.308	2.307	2.310	224.8	0.326	24.10	0.919	0.913
4	0.57	250	45	3.224	3.211	3.205	3.203	3.202	3.205	224.8	0.326	28.39	1.013	0.994
4.5	0.64	250	45	4.537	4.518	4.510	4.507	4.505	4.510	224.8	0.326	33.68	1.133	1.084

Table A2
Corner crack geometry correction factor calculations for different crack lengths from the 3D FE analyses at the surface and 45° locations around the crack front, top of model constrained, 7 × 7mm cross-section models

Crack length mm	a/w	Applied load MPa	Angle deg	J-integral values for contour no. MPa.mm					Av. J2-J5 MPa.mm	E GPa	Poisson's ratio	K MPa$\sqrt{m}$	Y	Y Pickard
				J1	J2	J3	J4	J5						
0.5	0.07	500	0	0.820	0.817	0.817	0.817	0.818	0.817	224.8	0.326	14.34	0.723	0.734
1	0.14	500	0	1.701	1.694	1.692	1.692	1.693	1.693	224.8	0.326	20.63	0.736	0.741
1.5	0.21	500	0	2.662	2.651	2.648	2.647	2.648	2.649	224.8	0.326	25.81	0.752	0.753
2	0.29	500	0	3.773	3.757	3.752	3.751	3.751	3.753	224.8	0.326	30.72	0.775	0.792
2.5	0.36	500	0	5.126	5.105	5.098	5.095	5.095	5.098	224.8	0.326	35.81	0.808	0.847
3	0.43	250	0	1.724	1.717	1.715	1.714	1.714	1.715	224.8	0.326	20.77	0.856	0.919
3.5	0.50	250	0	2.305	2.296	2.293	2.291	2.291	2.293	224.8	0.326	24.01	0.916	1.011
4	0.57	250	0	3.109	3.096	3.092	3.090	3.090	3.092	224.8	0.326	27.89	0.995	1.126
4.5	0.64	250	0	4.265	4.248	4.242	4.240	4.239	4.242	224.8	0.326	32.66	1.099	1.267
0.5	0.07	500	45	0.769	0.766	0.765	0.764	0.764	0.765	224.8	0.326	13.87	0.700	0.686
1	0.14	500	45	1.549	1.542	1.539	1.538	1.537	1.539	224.8	0.326	19.67	0.702	0.692
1.5	0.21	500	45	2.389	2.379	2.375	2.373	2.372	2.375	224.8	0.326	24.44	0.712	0.703
2	0.29	500	45	3.344	3.330	3.324	3.321	3.320	3.324	224.8	0.326	28.91	0.730	0.738
2.5	0.36	500	45	4.474	4.455	4.448	4.444	4.442	4.447	224.8	0.326	33.44	0.755	0.785
3	0.43	250	45	1.469	1.463	1.460	1.459	1.459	1.460	224.8	0.326	19.16	0.790	0.843
3.5	0.50	250	45	1.903	1.895	1.892	1.890	1.890	1.892	224.8	0.326	21.81	0.832	0.913
4	0.57	250	45	2.456	2.445	2.441	2.439	2.438	2.441	224.8	0.326	24.78	0.884	0.994
4.5	0.64	250	45	3.172	3.159	3.154	3.151	3.150	3.154	224.8	0.326	28.16	0.947	1.084

Table A3
Corner crack geometry correction factor values for a 4.5 mm crack in 7 × 7mm models of different lengths

Crack length mm	Applied load MPa	Model length mm	Constraint	Angle deg	J-integral values for contour no. MPa.mm					Av. J2-J5 MPa.mm	E GPa	Poisson's ratio	K MPa$\sqrt{m}$	Y
					J1	J2	J3	J4	J5					
		9	Free	0	6.583	6.557	6.547	6.543	6.542	6.547	224.8	0.326	40.58	1.365
		12.7	Free	0	6.557	6.532	6.522	6.518	6.517	6.522	224.8	0.326	40.50	1.363
		18	Free	0	6.557	6.531	6.521	6.517	6.516	6.521	224.8	0.326	40.50	1.362
		25.5	Free	0	6.557	6.531	6.521	6.517	6.516	6.521	224.8	0.326	40.50	1.362
		36	Free	0	6.557	6.531	6.521	6.517	6.516	6.521	224.8	0.326	40.50	1.362
		9	Free	45	4.561	4.543	4.535	4.531	4.529	4.535	224.8	0.326	33.77	1.136
		12.7	Free	45	4.537	4.519	4.511	4.507	4.505	4.511	224.8	0.326	33.68	1.133
		18	Free	45	4.537	4.518	4.510	4.507	4.505	4.510	224.8	0.326	33.68	1.133
		25.5	Free	45	4.537	4.518	4.510	4.507	4.505	4.510	224.8	0.326	33.68	1.133
4.5	250	36	Free	45	4.537	4.518	4.510	4.507	4.505	4.510	224.8	0.326	33.68	1.133
		9	Fixed	0	3.141	3.128	3.123	3.121	3.121	3.123	224.8	0.326	28.03	0.943
		12.7	Fixed	0	3.741	3.726	3.720	3.718	3.718	3.721	224.8	0.326	30.59	1.029
		18	Fixed	0	4.291	4.274	4.267	4.265	4.264	4.268	224.8	0.326	32.76	1.102
		25.5	Fixed	0	4.749	4.730	4.723	4.720	4.719	4.723	224.8	0.326	34.47	1.159
		36	Fixed	0	5.071	5.051	5.043	5.041	5.040	5.044	224.8	0.326	35.62	1.198
		9	Fixed	45	2.479	2.469	2.464	2.462	2.461	2.464	224.8	0.326	24.89	0.837
		12.7	Fixed	45	2.851	2.840	2.835	2.832	2.831	2.835	224.8	0.326	26.70	0.898
		18	Fixed	45	3.188	3.174	3.169	3.166	3.165	3.169	224.8	0.326	28.23	0.950
		25.5	Fixed	45	3.465	3.450	3.444	3.442	3.440	3.444	224.8	0.326	29.43	0.990
		36	Fixed	45	3.658	3.643	3.637	3.634	3.632	3.637	224.8	0.326	30.24	1.017

Table A4
Corner crack geometry correction factor calculations for different crack lengths from 3D FE analyses at the surface and 45° locations around the crack front, top of model free to deform, 10 × 10mm cross-section test piece B

Crack length mm	a/w	Applied load MPa	Angle deg	J-integral values for contour no. MPa.mm					Av. J2-J5 MPa.mm	E GPa	Poisson's ratio	K MPa$\sqrt{m}$	Y
				J1	J2	J3	J4	J5					
0.5	0.05	750	0	1.839	1.832	1.831	1.832	1.833	1.832	224.8	0.326	21.47	0.722
1	0.10	750	0	3.787	3.772	3.768	3.768	3.770	3.770	224.8	0.326	30.79	0.732
1.5	0.15	750	0	5.847	5.823	5.815	5.813	5.814	5.816	224.8	0.326	38.25	0.743
2	0.20	750	0	8.108	8.075	8.063	8.059	8.059	8.064	224.8	0.326	45.04	0.758
2.5	0.25	500	0	4.770	4.751	4.744	4.741	4.741	4.744	224.8	0.326	34.54	0.780
3	0.30	500	0	6.146	6.121	6.111	6.108	6.107	6.112	224.8	0.326	39.21	0.808
3.5	0.35	500	0	7.838	7.807	7.794	7.790	7.789	7.795	224.8	0.326	44.28	0.845
4	0.40	500	0	9.985	9.944	9.928	9.922	9.920	9.929	224.8	0.326	49.97	0.892
4.5	0.45	500	0	12.77	12.72	12.70	12.69	12.69	12.700	224.8	0.326	56.52	0.951
5	0.50	500	0	16.50	16.43	16.40	16.39	16.39	16.403	224.8	0.326	64.23	1.025
5.5	0.55	250	0	5.425	5.403	5.395	5.392	5.390	5.395	224.8	0.326	36.84	1.121
6	0.60	250	0	7.222	7.194	7.183	7.178	7.177	7.183	224.8	0.326	42.50	1.238
6.5	0.65	250	0	9.822	9.784	9.768	9.762	9.760	9.769	224.8	0.326	49.57	1.387
0.5	0.05	750	45	1.728	1.720	1.717	1.715	1.715	1.717	224.8	0.326	20.78	0.699
1	0.10	750	45	3.456	3.441	3.435	3.432	3.430	3.435	224.8	0.326	29.39	0.699
1.5	0.15	750	45	5.266	5.244	5.234	5.230	5.228	5.234	224.8	0.326	36.28	0.705
2	0.20	750	45	7.240	7.209	7.196	7.190	7.187	7.196	224.8	0.326	42.54	0.716
2.5	0.25	500	45	4.216	4.198	4.190	4.187	4.185	4.190	224.8	0.326	32.46	0.733
3	0.30	500	45	5.377	5.354	5.345	5.340	5.338	5.344	224.8	0.326	36.66	0.755
3.5	0.35	500	45	6.767	6.738	6.727	6.721	6.718	6.726	224.8	0.326	41.13	0.784
4	0.40	500	45	8.466	8.431	8.416	8.409	8.406	8.416	224.8	0.326	46.01	0.821
4.5	0.45	500	45	10.58	10.53	10.51	10.50	10.50	10.510	224.8	0.326	51.41	0.865
5	0.50	500	45	13.23	13.18	13.15	13.14	13.14	13.153	224.8	0.326	57.52	0.918
5.5	0.55	250	45	4.164	4.147	4.140	4.137	4.135	4.140	224.8	0.326	32.27	0.982
6	0.60	250	45	5.263	5.242	5.232	5.228	5.226	5.232	224.8	0.326	36.28	1.057
6.5	0.65	250	45	6.705	6.678	6.666	6.661	6.658	6.666	224.8	0.326	40.95	1.146

Table A5
Corner crack geometry correction factor calculations for different crack lengths from 3D FE analyses at the surface and 45° locations around the crack front, top of model free to deform, 5 × 5mm cross-section test piece C

Crack length mm	a/w	Applied load MPa	Angle deg	J-integral values for contour no. MPa.mm					Av. J2-J5 MPa.mm	E GPa	Poisson's ratio	K MPa$\sqrt{m}$	Y
				J1	J2	J3	J4	J5					
0.5	0.10	500	0	0.826	0.823	0.823	0.823	0.824	0.823	224.8	0.326	14.39	0.726
1	0.20	500	0	1.782	1.775	1.773	1.773	1.774	1.774	224.8	0.326	21.12	0.754
1.5	0.30	500	0	3.041	3.029	3.025	3.025	3.025	3.026	224.8	0.326	27.59	0.804

(*continued on next page*)

Table A5 (*continued*)

Crack length mm	a/w	Applied load MPa	Angle deg	J-integral values for contour no. MPa.mm					Av. J2-J5 MPa.mm	E GPa	Poisson's ratio	K MPa$\sqrt{m}$	Y
				J1	J2	J3	J4	J5					
2	0.40	250	0	1.243	1.238	1.236	1.236	1.236	1.237	224.8	0.326	17.64	0.890
2.5	0.50	250	0	2.059	2.051	2.048	2.047	2.047	2.048	224.8	0.326	22.70	1.024
3	0.60	250	0	3.592	3.578	3.573	3.571	3.571	3.573	224.8	0.326	29.98	1.235
3.5	0.70	250	0	6.830	6.803	6.793	6.790	6.789	6.794	224.8	0.326	41.34	1.577
0.5	0.10	500	45	0.775	0.771	0.770	0.769	0.769	0.770	224.8	0.326	13.92	0.702
1	0.20	500	45	1.619	1.612	1.609	1.608	1.607	1.609	224.8	0.326	20.12	0.718
1.5	0.30	500	45	2.698	2.687	2.682	2.680	2.679	2.682	224.8	0.326	25.97	0.757
2	0.40	250	45	1.063	1.059	1.057	1.056	1.056	1.057	224.8	0.326	16.30	0.823
2.5	0.50	250	45	1.662	1.655	1.652	1.651	1.650	1.652	224.8	0.326	20.38	0.920
3	0.60	250	45	2.639	2.628	2.623	2.621	2.620	2.623	224.8	0.326	25.69	1.058
3.5	0.70	250	45	4.328	4.310	4.303	4.300	4.298	4.303	224.8	0.326	32.90	1.255

Table A6
Corner crack geometry correction factor calculations for different crack lengths from 3D FE analyses at the surface and 45° locations around the crack front, top of model constrained, 10 × 10mm cross-section test piece B

Crack length mm	a/w	Applied load MPa	Angle deg	J-integral values for contour no. MPa.mm					Av. J2-J5 MPa.mm	E GPa	Poisson's ratio	K MPa$\sqrt{m}$	Y
				J1	J2	J3	J4	J5					
0.5	0.05	750	0	1.838	1.831	1.830	1.831	1.832	1.831	224.8	0.326	21.46	0.722
1	0.10	750	0	3.771	3.756	3.752	3.752	3.754	3.754	224.8	0.326	30.73	0.731
1.5	0.15	750	0	5.769	5.746	5.738	5.736	5.737	5.739	224.8	0.326	37.99	0.738
2	0.20	750	0	7.875	7.843	7.831	7.828	7.828	7.833	224.8	0.326	44.38	0.747
2.5	0.25	500	0	4.527	4.508	4.502	4.499	4.499	4.502	224.8	0.326	33.65	0.759
3	0.30	500	0	5.650	5.627	5.618	5.615	5.615	5.619	224.8	0.326	37.59	0.774
3.5	0.35	500	0	6.921	6.892	6.882	6.878	6.877	6.882	224.8	0.326	41.61	0.794
4	0.40	500	0	8.389	8.355	8.341	8.336	8.335	8.342	224.8	0.326	45.80	0.817
4.5	0.45	500	0	10.12	10.08	10.06	10.06	10.05	10.063	224.8	0.326	50.31	0.846
5	0.50	500	0	12.20	12.15	12.13	12.12	12.12	12.130	224.8	0.326	55.23	0.881
5.5	0.55	250	0	3.711	3.696	3.690	3.688	3.687	3.690	224.8	0.326	30.47	0.927
6	0.60	250	0	4.514	4.496	4.489	4.487	4.486	4.490	224.8	0.326	33.60	0.979
6.5	0.65	250	0	5.540	5.518	5.509	5.506	5.504	5.509	224.8	0.326	37.22	1.042
0.5	0.05	750	45	1.727	1.719	1.716	1.714	1.714	1.716	224.8	0.326	20.77	0.699
1	0.10	750	45	3.441	3.426	3.420	3.417	3.416	3.420	224.8	0.326	29.33	0.698
1.5	0.15	750	45	5.198	5.176	5.167	5.163	5.161	5.167	224.8	0.326	36.05	0.700
2	0.20	750	45	7.040	7.010	6.997	6.992	6.989	6.997	224.8	0.326	41.95	0.706
2.5	0.25	500	45	4.011	3.994	3.987	3.984	3.982	3.987	224.8	0.326	31.67	0.715
3	0.30	500	45	4.969	4.949	4.940	4.936	4.934	4.940	224.8	0.326	35.25	0.726
3.5	0.35	500	45	6.032	6.007	5.996	5.991	5.989	5.996	224.8	0.326	38.83	0.741
4	0.40	500	45	7.227	7.197	7.185	7.179	7.176	7.184	224.8	0.326	42.51	0.758
4.5	0.45	500	45	8.587	8.551	8.536	8.529	8.526	8.536	224.8	0.326	46.33	0.779
5	0.50	500	45	10.15	10.11	10.09	10.08	10.08	10.090	224.8	0.326	50.38	0.804
5.5	0.55	250	45	3.003	2.991	2.986	2.983	2.982	2.986	224.8	0.326	27.40	0.834
6	0.60	250	45	3.541	3.526	3.520	3.517	3.516	3.520	224.8	0.326	29.75	0.867
6.5	0.65	250	45	4.180	4.163	4.156	4.152	4.151	4.156	224.8	0.326	32.33	0.905

Table A7
Corner crack geometry correction factor calculations for different crack lengths from 3D FE analyses at the surface and 45° locations around the crack front, top of model constrained, 5 × 5mm cross-section test piece C

Crack length mm	a/w	Applied load MPa	Angle deg	J-integral values for contour no. MPa.mm					Av. J2-J5 MPa.mm	E GPa	Poisson's ratio	K MPa$\sqrt{m}$	Y
				J1	J2	J3	J4	J5					
0.5	0.10	500	0	0.824	0.821	0.821	0.821	0.821	0.821	224.8	0.326	14.37	0.725
1	0.20	500	0	1.752	1.745	1.743	1.743	1.744	1.744	224.8	0.326	20.94	0.747
1.5	0.30	500	0	2.893	2.881	2.877	2.876	2.877	2.878	224.8	0.326	26.90	0.784
2	0.40	250	0	1.122	1.118	1.116	1.116	1.116	1.117	224.8	0.326	16.76	0.846
2.5	0.50	250	0	1.719	1.712	1.710	1.709	1.709	1.710	224.8	0.326	20.74	0.936
3	0.60	250	0	2.693	2.682	2.678	2.677	2.677	2.679	224.8	0.326	25.96	1.069
3.5	0.70	250	0	4.416	4.399	4.392	4.390	4.389	4.393	224.8	0.326	33.24	1.268
0.5	0.10	500	45	0.773	0.769	0.768	0.767	0.767	0.768	224.8	0.326	13.90	0.701
1	0.20	500	45	1.592	1.585	1.583	1.581	1.581	1.583	224.8	0.326	19.95	0.712
1.5	0.30	500	45	2.575	2.564	2.559	2.557	2.556	2.559	224.8	0.326	25.37	0.739
2	0.40	250	45	0.969	0.965	0.963	0.963	0.962	0.963	224.8	0.326	15.57	0.786
2.5	0.50	250	45	1.418	1.413	1.410	1.409	1.408	1.410	224.8	0.326	18.83	0.850
3	0.60	250	45	2.066	2.057	2.054	2.052	2.051	2.054	224.8	0.326	22.73	0.936
3.5	0.70	250	45	3.033	3.020	3.015	3.013	3.012	3.015	224.8	0.326	27.54	1.050

Table A8
Comparison of FE and predicted geometry correction factor values for the three test piece designs, model tops constrained

Model width mm	Crack length a mm	a/w	Model length mm	Lequiv 3D mm	YLfac0	YLfac45	FE Y0 fix	FE Y45 fix	Cal Y0	Cal Y45	% diff Y0	% diff Y45
5	0.5	0.10	16.75	23.45	1.139	1.137	0.725	0.701	0.732	0.697	0.90	−0.60
5	1.0	0.20	16.75	23.45	1.139	1.137	0.747	0.712	0.752	0.713	0.58	0.19
5	1.5	0.30	16.75	23.45	1.139	1.137	0.784	0.739	0.789	0.742	0.64	0.39
5	2.0	0.40	16.75	23.45	1.139	1.137	0.846	0.786	0.849	0.786	0.44	0.08
5	2.5	0.50	16.75	23.45	1.139	1.137	0.936	0.850	0.942	0.849	0.59	−0.06
5	3.0	0.60	16.75	23.45	1.139	1.137	1.069	0.936	1.076	0.937	0.65	0.08
5	3.5	0.70	16.75	23.45	1.139	1.137	1.268	1.050	1.267	1.055	−0.08	0.44
7	0.5	0.07	17.69	17.69	1.003	0.997	0.723	0.700	0.728	0.694	0.65	−0.79
7	1.0	0.14	17.69	17.69	1.003	0.997	0.736	0.702	0.737	0.701	0.07	−0.10
7	1.5	0.21	17.69	17.69	1.003	0.997	0.752	0.712	0.752	0.714	0.02	0.21
7	2.0	0.29	17.69	17.69	1.003	0.997	0.775	0.730	0.775	0.732	0.03	0.27
7	2.5	0.36	17.69	17.69	1.003	0.997	0.808	0.755	0.809	0.756	0.07	0.18
7	3.0	0.43	17.69	17.69	1.003	0.997	0.856	0.790	0.854	0.789	−0.15	−0.14
7	3.5	0.50	17.69	17.69	1.003	0.997	0.916	0.832	0.916	0.830	−0.04	−0.23
7	4.0	0.57	17.69	17.69	1.003	0.997	0.995	0.884	0.996	0.883	0.09	−0.17
7	4.5	0.64	17.69	17.69	1.003	0.997	1.099	0.947	1.099	0.948	0.05	0.03
10	0.5	0.05	18.30	12.81	0.810	0.800	0.722	0.699	0.727	0.693	0.63	−0.86
10	1.0	0.10	18.30	12.81	0.810	0.800	0.731	0.698	0.730	0.696	−0.15	−0.30
10	1.5	0.15	18.30	12.81	0.810	0.800	0.738	0.700	0.736	0.700	−0.32	0.01
10	2.0	0.20	18.30	12.81	0.810	0.800	0.747	0.706	0.744	0.707	−0.34	0.19
10	2.5	0.25	18.30	12.81	0.810	0.800	0.759	0.715	0.755	0.716	−0.51	0.17
10	3.0	0.30	18.30	12.81	0.810	0.800	0.774	0.726	0.770	0.727	−0.51	0.14
10	3.5	0.35	18.30	12.81	0.810	0.800	0.794	0.741	0.790	0.741	−0.50	0.07
10	4.0	0.40	18.30	12.81	0.810	0.800	0.817	0.758	0.814	0.758	−0.45	−0.02
10	4.5	0.45	18.30	12.81	0.810	0.800	0.846	0.779	0.843	0.779	−0.37	−0.09
10	5.0	0.50	18.30	12.81	0.810	0.800	0.881	0.804	0.879	0.803	−0.26	−0.13
10	5.5	0.55	18.30	12.81	0.810	0.800	0.927	0.834	0.923	0.831	−0.47	−0.30
10	6.0	0.60	18.30	12.81	0.810	0.800	0.979	0.867	0.975	0.865	−0.41	−0.27
10	6.5	0.65	18.30	12.81	0.810	0.800	1.042	0.905	1.037	0.903	−0.47	−0.20

References

[1] A.C. Pickard, The Application of 3-dimensional Finite Element Methods to Fracture Mechanics and Fatigue Life Prediction, Chameleon Press, London, 1986.
[2] J.C. Newman Jr., I.S. Raju, Stress-intensity factor equations for cracks in three-dimensional finite bodies, in: J.C. Lewis, G. Sines (Eds.), Fracture Mechanics: Fourteenth Symposium – Volume 1: Theory and Analysis, ASTM STP-791, American Society for Testing and Materials, 1983, pp. 238–265.
[3] I.S. Raju, J.C. Newman Jr., in: T.A. Cruse (Ed.), Stress-intensity Factors for Corner Cracks in Rectangular Bars, ed.Fracture Mechanics: Nineteenth Symposium (STP969-EB, ASTM International, 1988.
[4] EN 3873, Test Methods for Metallic Materials. Determination of Fatigue Crack Growth Using Corner-Crack (CC) Test Pieces, Aerospace series, 2010.
[5] R.F. Hall, B.E. Powell, The growth of corner cracks by fatigue, Int. J. Fatig. 19 (5) (1997) 429–435.
[6] G. Onofrio, G.A. Osinkolu, M. Marchionni, Effects of loading waveform on fatigue crack growth of Udimet 720 Li superalloy, Int. J. Fatig. 26 (2004) 203–209.
[7] S. Boljanović, A. Carpinteri, Computational analysis of a surface corner crack under cyclic loading, Procedia Struct. Integr. 28 (2020) 2370–2377.
[8] T. Tinga, Stress intensity factors and crack propagation in a single crystal nickel-based superalloy, Eng. Fract. Mech. 73 (2006) 1679–1692.
[9] A. Koko, S. Singh, S. Barhli, T. Connolley, N.T. Vo, T. Wigger, D. Liu, Y. Fu, J. Rethoré, J. Lechambre, J.-Y. Buffiere, T.J. Marrow, 3-Dimensional analysis of fatigue crack fields and crack growth by in situ synchrotron X-ray tomography, Int. J. Fatig. 170 (2023), 107541.
[10] P. Catalin Iliea, A. Incea, A. Loghin, Assessment of fatigue crack growth based on 3D finite element modeling approach, Procedia Struct. Integr. 38 (2022) 271–282.
[11] P.R. Heyllger, On conventional and quarter-point mixed elements in linear elastic fracture mechanics, Eng. Fract. Mech. 31 (1988) 157–171.
[12] K. Rege, H.G. Lemu, A review of fatigue crack propagation modelling techniques using FEM and XFEM, IOP Conf. Ser. Mater. Sci. Eng. 276 (2017), 012027.
[13] ABAQUS/CAE, User Manual, Dassault Systèmes, 2021.
[14] J. Toribio, B. González, J.-C. Matos, Mulas Ó, Stress intensity factors for embedded, surface, and corner cracks in finite-thickness plates subjected to tensile loading, Materials 14 (11) (2021) 2807, https://doi.org/10.3390/ma14112807.
[15] L. Zhao, J. Tong, J. Byrne, Stress intensity factor K and the elastic T-stress for corner cracks, Int. J. Fract. 109 (2001) 209–225.
[16] J. Toribio, B. González, J.-C. Matos, O. Mulas, Stress intensity factors for embedded, surface, and corner cracks in finite-thickness plates subjected to tensile loading, Materials 14 (2021) 2807.
[17] S.H. Crandall, N.C. Dahl, T.J. Lardner, An Introduction to the Mechanics of Solids, International student edition, McGraw Hill, New York, 1978.
[18] A.M. Howatson, P.G. Lund, J.D. Todd, Engineering Tables and Data, first ed., Chapman and Hall, London, 1982.